MOX-Report No. 36/2017

Mathematical modelling, analysis and numerical approximation of second order elliptic problems with inclusions

Koeppl, T.; Vodotto, E.; Wohlmuth, B.; Zunino, P.

MOX, Dipartimento di Matematica
Politecnico di Milano, Via Bonardi 9 - 20133 Milano (Italy)

mox-dmat@polimi.it http://mox.polimi.it

Mathematical Models and Methods in Applied Sciences

Mathematical modelling, analysis and numerical approximation of second order elliptic problems with inclusions

Tobias Köppl

Department of Hydromechanics and Modelling of Hydrosystems, University of Stuttgart, Pfaffenwaldring 61, 70569 Stuttgart, Germany
tobias.koeppl@iws.uni-stuttgart.de

Ettore Vidotto*, Barbara Wohlmuth

Lehrstuhl für Numerische Mathematik, University of Technology Munich, Boltzmannstraße 3, 85748 Garching, Germany
ettore.vidotto@ma.tum.de, barbara.wohlmuth@ma.tum.de

Paolo Zunino

MOX, Politecnico di Milano, via Bonardi 9, 20133 Milano, Italy
paolo.zunino@polimi.it

Received (Day Month Year)
Revised (Day Month Year)

Many biological and geological systems can be modelled as porous media with small inclusions. Vascularized tissue, roots embedded in soil or fractured rocks are examples of such systems. In these applicatons, tissue, soil or rocks are considered to be porous media, while blood vessels, roots or fractures form small inclusions. To model flow processes in thin inclusions, one-dimensional (1D) models of Darcy- or Poiseuille type have been used, whereas Darcy-equations of higher dimension have been considered for the flow processes within the porous matrix. A coupling between flow in the porous matrix and the inclusions can be achieved by setting suitable source terms for the corresponding models, where the source term of the higher-dimensional model is concentrated on the centre lines of the inclusions.

In this paper, we investigate an alternative coupling scheme. Here, the source term lives on the boundary of the inclusions. By doing so, we lift the dimension by one and thus increase the regularity of the solution. We show that this model can be derived from a full-dimensional model and the occurring modelling errors are estimated. Furthermore, we prove the well-posedness of the variational formulation and discuss the convergence behaviour of standard finite element methods with respect to this model. Our theoretical results are confirmed by numerical tests. Finally, we demonstrate how the new coupling concept can be used to simulate stationary flow through a capillary network embedded in a biological tissue.

Keywords: elliptic problems, small inclusions, model reduction, finite element approximation.

AMS Subject Classification: 78M34, 65N30, 65N12, 65N15

1. Introduction

In this work, we address a special type of second order elliptic equation, which can be considered a model problem for diffusion processes in porous media with small inclusions. To define this problem, a two-dimensional, open, bounded and convex domain $\Omega \subset \mathbb{R}^2$ is considered. Moreover, we assume that Ω is a polygonal domain. Within Ω there are $N \in \mathbb{N}$ open balls $B_i \subset \Omega$. By B_i, we denote a ball around a centre $x_i \in \Omega$ having the radius R_i. For a given constant $C > 0$ it holds:

$$\operatorname{dist}(\partial\Omega, B_j) > C,\ \operatorname{dist}(B_i, B_j) > C,\ i \neq j,\ i, j \in \{1, \dots, N\},$$

where

$$\operatorname{dist}(M, B_j) = \min\left\{ \|x - y\|_2 |\ x \in \overline{M},\ y \in \overline{B}_j \right\},\ M \in \{\partial\Omega, B_i\}.$$

For notational convenience, we split the domain Ω in two parts, Ω_f, Ω_p:

$$\Omega_p = \Omega \setminus \overline{\Omega}_f,\ \text{where } \Omega_f = \bigcup_{i=1}^{N} B_i. \tag{1.1}$$

In the applications discussed in more detail later on, Ω_f represents the collection of channels and fractures, while Ω_p is the surrounding porous material. Having this notation at hand, our model problem reads as follows:

$$-\Delta u_{\text{ref}} = f \text{ in } \Omega_p,\ -\nabla u_{\text{ref}} \cdot n_i = \kappa_i (U_i - u_{\text{ref}}) \text{ on } \partial B_i,\ u_{\text{ref}} = 0 \text{ on } \partial\Omega. \tag{1.2}$$

The source term $f \in L^2(\Omega_p)$ represents a body force or external source and sink terms, while $\kappa_i (U_i - u_{\text{ref}})$ is modelling a flux through the interface Γ_i from the inclusions into the porous medium or vice versa. More precisely, $\kappa_i \in \mathbb{R},\ \kappa_i > 0$ plays the role of a permeability, $U_i \in \mathbb{R},\ U_i > 0$ is a given intensity of the inclusion Ω_i, and n_i denotes the outward unit normal vector of ∂B_i. In Section 7, we will also consider the case where U_i are functions that obey partial differential equations coupled with problem (1.2). For applications with many small inclusions, model (1.2) is computationally unfeasible, because of the excessive computational cost that would arise using a computational mesh that conforms to all inclusions. Therefore, we present in this work a simplified form of problem (1.2), which considerably reduces the cost of numerical simulations. The reduced model we propose consists of the following equations for the unknown u_{red}:

$$-\Delta u_{\text{red}} = \mathcal{F} + \sum_{i=1}^{N} \kappa_i \left(U_i - \overline{u}_{\text{red}}^{(i)} \right) \delta_{\partial B_i} \text{ in } \Omega, \quad u_{\text{red}} = 0 \text{ on } \partial\Omega, \tag{1.3}$$

where $\delta_{\partial B_i}$ stands for a Dirac measure laying on ∂B_i and the expression $\overline{u}_{\text{red}}^{(i)}$ abbreviates the mean value of u_{red} on ∂B_i:

$$\overline{u}_{\text{red}}^{(i)} = \frac{1}{2\pi R_i} \int_{\partial B_i} u_{\text{red}}\, dS. \tag{1.4}$$

The fluctuations $\tilde{u}_{\text{red}}^{(i)}$ of u_{red} on ∂B_i are defined by:

$$\tilde{u}_{\text{red}}^{(i)} = u_{\text{red}}|_{\partial B_i} - \overline{u}_{\text{red}}^{(i)}. \tag{1.5}$$

The source term $\mathcal{F} \in L^2(\Omega)$ is an extension of the source term f in (1.2), where we claim that $\mathcal{F}$ coincides with f on Ω_p:

$$\mathcal{F}(x) = \begin{cases} f(x), & \text{for } x \in \Omega_p, \\ f_i(x), & \text{for } x \in B_i. \end{cases} \tag{1.6}$$

In addition to that, it may hold that $\mathcal{F}$ exhibits no jumps at the interfaces ∂B_i and that for a constant $C_f > 0$:

$$\|f_i\|_{L^2(B_i)} \leq C_f \|f\|_{L^2(\Omega_p)}, \quad \forall i \in \{1, \ldots, N\}. \tag{1.7}$$

In cases where U_i are the solutions of partial differential equations derived from model reduction techniques, thus defined on lower dimensional manifolds or sets (2D,1D,0D), this gives rise to coupled systems of PDEs defined on embedded domains with heterogeneous dimensionality[5,7,26,14]. Such PDE systems are often classified into PDE systems with co-dimension 1, i.e., 3D-2D or 2D-1D coupled PDEs, and PDEs with co-dimension 2, i.e., 3D-1D or 2D-0D coupled problems.

The numerical analysis and discretization of these types of problems have been investigated in several publications [6,17,20]. For the numerical treatment of interface problems with co-dimension 1, XFEM methods have proved to be very effective [10,32]. In the case of co-dimension 2, the solution of the higher dimensional problem exhibits singularities along the manifolds representing the inclusions. When the lower dimensional problems are represented as a distribution of Dirac source terms embedded into the higher dimensional space, the reduced regularity deteriorates the convergence of numerical methods and optimal convergence rates can only be recovered using graded meshes or local error norms [2,6,19,18].

In this paper, we investigate by means of the model problem (1.3) a different way of coupling partial differential equations with heterogeneous dimensionality. The fundamental difference between the coupling term in (1.3) and the existing coupling concepts is that the inclusion is not represented by a single line or point in space. In the source term of (1.3) the Dirac measure is concentrated on the physical boundary of the inclusions. Therefore, a dimensional gap of two in the coupling term is avoided and the corresponding solution is smoother. At the same time, the averaging technique applied to the interface conditions makes it possible to couple the bulk problem with sub-problems defined on manifolds of co-dimension two. This formulation allows for a more natural mathematical analysis of the model, numerical discretization and error analysis of the resulting approximation schemes.

The coupling of three-dimensional continua with embedded 1D inclusions, of which the proposed model represents a template, arises in applications of great importance such as microcirculation, flow through perforated media and the study of reinforced materials.

Flow and transport simulations in complex vascular networks are becoming a popular approach to studing the physiology of tumors and to design new treatments [12,25,34]. This new trend is motivated by the need to incorporate accurate physical models of flow, biochemical transport and mechanical interactions within a realistic

geometrical description of the vasculature, which in turn enables the comparison of simulations with imaging data captured at the microscale by means of intravital microscopy techniques [3,4,22,23,36]. We also point out that a similar approach is being used for simulating the interaction of plant roots with soil [31].

This new approach for solving PDEs in domains with inclusions is also of interest in many other fields such as in the design of cooling systems for electronics (for designing pulsating heat pipes for space applications) in neuroscience (to study the impact of cerebrospinal fluid clearance on chronic mental disease and dementia) and in the simulation of floods (through the interaction of the hydraulic network with the surrounding territory).

The remaining parts of this work are organized as follows: In Section 2, we summarize some trace inequalities which are required for the mathematical analysis in the following sections. Section 3 presents the model derivation and the weak formulation of (1.3). Moreover, the existence and uniqueness of the weak solution is shown and its regularity is discussed. Section 4 characterizes the modelling error. In Section 5, we consider the numerical discretization by the finite element method and study its convergence. Our theoretical results are confirmed by numerical tests, which are presented in Section 6. Finally, in Section 7, the new coupling concept is used to address a relevant application, i.e., the perfusion of vascularized biological tissues.

2. Trace inequalities

In this section, we discuss two trace inequalities that are key ingredients for our mathematical analysis. The first trace inequality allows us to bound the mean value $\overline{v}^{(i)}$ (see (1.4)) of a function $v \in H_0^1(\Omega)$ with respect to the boundary of a ball B_i, while the second trace inequality is an inequality of Steklov-type providing an upper bound for traces of functions v, whose averages vanish on ∂B_i:

$$\int_{\partial B_i} v \, dS = 0.$$

In order to prove the well-posedness of our model problem (Section 3) and to derive suitable upper bounds for the modelling error (Section 4), it is crucial to know how the arising constants depend on the radii R_i of the circular inclusions B_i. Therefore, we investigate these constants in more details.

Lemma 2.1. *Let $B_i \subset \Omega$ be a ball with a sufficiently small radius R_i. Then it holds for the mean value $\overline{v}^{(i)}$ of $v \in H_0^1(\Omega)$:*

$$\overline{v}^{(i)} \leq C \left|\ln R_i\right|^{\frac{1}{2}} \|\nabla v\|_{L^2(\Omega)},$$

where the constant $C > 0$ is independent of R_i.

Proof. According to [1][Remark 1], it holds for B_i:

$$\overline{v}^{(i)} \leq \frac{1}{2\pi R_i} \left(\frac{2}{R_i} \int_{B_i} |v| \, dx + \int_{B_i} |\nabla v| \, dx \right).$$

Applying the Hölder inequality to both summands, we have:

$$\begin{aligned}\overline{v}^{(i)} &\leq \frac{1}{\pi R_i^2}\left(\pi R_i^2\right)^{\frac{1}{q}} \|v\|_{L^p(B_i)} + \frac{\sqrt{\pi R_i^2}}{2\pi R_i}\|\nabla v\|_{L^2(B_i)}\,,\\ &\leq \left(\pi R_i^2\right)^{-\frac{1}{p}} \|v\|_{L^p(B_i)} + \frac{\sqrt{\pi R_i^2}}{2\pi R_i}\|\nabla v\|_{L^2(B_i)}\,.\end{aligned}$$

for the parameters p and q such that $1/p+1/q=1$, while the L^1-norm in the second summand is estimated by a product of L^2-norms. The choice $p=|\ln R_i|\geq 2$ and $q=\frac{|\ln R_i|}{|\ln R_i|-1}$ yields:

$$\begin{aligned}\overline{v}^{(i)} &\leq \pi^{-\frac{1}{|\ln R_i|}} R_i^{-\frac{2}{|\ln R_i|}} \|v\|_{L^p(B_i)} + \frac{\sqrt{\pi R_i^2}}{2\pi R_i}\|\nabla v\|_{L^2(B_i)}\\ &\leq \exp(2)\,\|v\|_{L^p(\Omega)} + \frac{1}{2\sqrt{\pi}}\|\nabla v\|_{L^2(\Omega)}\,.\end{aligned}$$

According to a Sobolev inequality [37] [Equation (6.20)], there exists a constant $C>0$ independent of R_i such that for $v\in H_0^1(\Omega)$ it holds true:

$$\|v\|_{L^p(\Omega)} \leq C p^{\frac{1}{2}}\|\nabla v\|_{L^2(\Omega)}\,. \tag{2.1}$$

Therefore, we have

$$\overline{v}^{(i)} \leq C\left(|\ln R_i|^{\frac{1}{2}}\|\nabla v\|_{L^2(\Omega)} + \|\nabla v\|_{L^2(\Omega)}\right),$$

with a constant $C>0$ independent of R_i. □

Next, we derive by means of the Steklov inequality a trace inequality for the fluctuation $\tilde{v}^{(i)}$ with respect to a ball B_i (see (1.5)).

Lemma 2.2. *Let $B_i\subset\mathbb{R}^2$ be a ball with a sufficiently small radius R_i and $v\in H_0^1(\Omega)$. Then we have:*

$$\|v\|_{L^2(\partial B_i)} \leq C\sqrt{R_i\,|\ln R_i|}\,\|\nabla v\|_{L^2(\Omega)}\,,$$

where $C>0$ is a constant independent of R_i.

Proof. Observing that $\int_{\partial B_i}\tilde{v}^{(i)}\,dS=0$, we find in terms of [16] [Section 3] and [21] [Section 5] that

$$\left\|\tilde{v}^{(i)}\right\|_{L^2(\partial B_i)} \leq \sqrt{R_i}\,\|\nabla v\|_{L^2(B_i)}\,. \tag{2.2}$$

Using the orthogonal decomposition of v, we obtain:

$$\|v\|^2_{L^2(\partial B_i)} = \left\|\overline{v}^{(i)}+\tilde{v}^{(i)}\right\|^2_{L^2(\partial B_i)} = 2\pi R_i\left(\overline{v}^{(i)}\right)^2 + \left\|\tilde{v}^{(i)}\right\|^2_{L^2(\partial B_i)}\,.$$

In order to bound the first term, we apply Lemma 2.1 and the second term is bounded by (2.2). □

3. Model derivation and analysis

Let us start with the variational formulation of reference problem (1.2). It consists of finding $u_{\text{ref}} \in V(\Omega_p)$ such that

$$(\nabla u_{\text{ref}}, \nabla v)_{\Omega_p} + \sum_{i=1}^{N} \kappa_i (u_{\text{ref}}, v)_{\partial B_i} = (f, v)_{\Omega_p} + \sum_{i=1}^{N} \kappa_i U_i \int_{\partial B_i} v \, dS, \quad \forall v \in V(\Omega_p), \tag{3.1}$$

where we have adopted the standard notation for the L^2-inner product. The function space $V(\Omega_p)$ is defined as follows:

$$V(\Omega_p) = \left\{ v \in H^1(\Omega_p) \mid v|_{\partial\Omega} = 0 \right\}.$$

Using (1.4) and (1.5), the interface terms can be written as:

$$(u, v)_{\partial B_i} = \int_{\partial B_i} u \, v \, dS = 2\pi R_i \, \overline{u}^{(i)} \overline{v}^{(i)} + \int_{\partial B_i} \widetilde{u}^{(i)} \, \widetilde{v}^{(i)} dS. \tag{3.2}$$

We derive a simplified model (also named here as *reduced model*) on the basis of the following assumptions, which rely on the fact that the inclusions are small:

(A1) we identify the domain Ω_p with the entire Ω;

(A2) we assume that the residual term in (3.2) is small, namely

$$\int_{\partial B_i} \widetilde{u}^{(i)} \, \widetilde{v}^{(i)} dS \simeq 0.$$

In Section 4, we will define the error components associated with each of these assumptions, and we will analyse their magnitude in terms of the parameters of the problem. We replace (3.1) with a surrogate problem: Find $u_{\text{red}} \in H_0^1(\Omega)$ such that

$$(\nabla u_{\text{red}}, \nabla v)_{\Omega} + 2\pi \sum_{i=1}^{N} R_i \kappa_i \overline{u}_{\text{red}}^{(i)} \overline{v}^{(i)} = (\mathcal{F}, v)_{\Omega} + 2\pi \sum_{i=1}^{N} R_i \kappa_i U_i \overline{v}^{(i)}, \quad \forall v \in H_0^1(\Omega). \tag{3.3}$$

Problem (3.3) is equivalent to finding $u_{\text{red}} \in H_0^1(\Omega)$ such that:

$$a(u_{\text{red}}, v) = L(v), \quad \forall v \in H_0^1(\Omega), \tag{3.4}$$

where the bilinear form $a(\cdot, \cdot) : H_0^1(\Omega) \times H_0^1(\Omega) \to \mathbb{R}$ is given by:

$$a(u, v) = (\nabla u, \nabla v)_{\Omega} + 2\pi \sum_{i=1}^{N} R_i \kappa_i \overline{u}^{(i)} \, \overline{v}^{(i)}. \tag{3.5}$$

The linear form L is defined as follows:

$$L : H_0^1(\Omega) \to \mathbb{R}, \quad L(v) = (\mathcal{F}, v)_{\Omega} + 2\pi \sum_{i=1}^{N} R_i \kappa_i U_i \, \overline{v}^{(i)}. \tag{3.6}$$

Obviously, (3.4) is the weak formulation of the reduced problem (1.3). For the variational problem (3.4), one can prove the following result on the well-posedness:

Theorem 3.1. *Let the requirements of Lemma 2.1 be fulfilled. Then problem* (3.4) *has a unique solution*

$$u_{\text{red}} \in H_0^1(\Omega) \cap H^{\frac{3}{2}-\epsilon}(\Omega),\ \forall \epsilon > 0.$$

Furthermore it holds the following stability estimate:

$$\|u_{\text{red}}\|_{H_0^1(\Omega)} \leq C \left(\|\mathcal{F}\|_{L^2(\Omega)} + \sum_{i=1}^{N} \kappa_i R_i |\ln R_i|^{\frac{1}{2}} U_i \right).$$

Proof. The variational problem (3.4) can be analysed by means of the Lax-Milgram Lemma. We begin by proving that the symmetric bilinear form (3.5) is continuous and coercive. The coercivity is a direct consequence of the Poincaré inequality. More precisely for any $v \in H_0^1(\Omega)$ there exists a positive constant C_P independent of R_i and κ_i, such that:

$$a(v,v) \geq (\nabla v, \nabla v)_\Omega \geq \left(1 + C_P^2\right)^{-1} \|v\|^2_{H_0^1(\Omega)}.$$

By means of Lemma 2.1, we have

$$2\pi R_i\, \overline{u}^{(i)}\, \overline{v}^{(i)} \leq 2\pi R_i C\, |\ln R_i|\, \|u\|_{H_0^1(\Omega)}\, \|v\|_{H_0^1(\Omega)}. \tag{3.7}$$

Then, using (3.7), we obtain the continuity of the bilinear form:

$$a(u,v) \leq \left(1 + 2\pi C \sum_{i=1}^{N} \kappa_i R_i\, |\ln R_i|\right) \|u\|_{H_0^1(\Omega)}\ \|v\|_{H_0^1(\Omega)}.$$

The boundedness of the linear form (3.6) then remains to be proven. According to Lemma 2.1 we have:

$$2\pi R_i \overline{v}^{(i)} \leq 2\pi R_i C\, |\ln R_i|^{\frac{1}{2}}\, \|\nabla v\|_{L^2(\Omega)} \leq 2\pi R_i C\, |\ln R_i|^{\frac{1}{2}}\, \|v\|_{H_0^1(\Omega)}.$$

All in all, it follows that there is a unique solution $u_{\text{red}} \in H_0^1(\Omega)$. Due to the presence of Dirac source terms in (1.3) no H^2-regularity can be recovered and the question arises as to which interspace $\tilde{V}$ with $H^2(\Omega) \subset \tilde{V} \subset H_0^1(\Omega)$ the solution u_{red} belongs. Since the right hand side in (1.3) is in $H^{-\frac{1}{2}-\epsilon}(\Omega),\ \forall \epsilon > 0$ it can be shown, analogous to Case (iii) in [15] [Theorem 2.1], that $u_{\text{red}} \in H^{\frac{3}{2}-\epsilon}(\Omega),\ \forall \epsilon > 0$. Testing (3.4) with $v = u_{\text{red}}$, using the coercivity of the bilinear form a, the continuity result of the linear form L and the Cauchy-Schwarz inequality the above stability estimate can be derived.

□

4. Analysis of the modelling error

We aim to analyse the error arising from assumptions (A1) and (A2) at the basis of the reduced model (3.3). Let us denote by u_{int} the solution of the problem obtained after the intermediate step (A1), that is

$$(\nabla u_{\text{int}}, \nabla v)_\Omega + \sum_{i=1}^{N} \kappa_i (u_{\text{int}}, v)_{\partial B_i} = (\mathcal{F}, v)_\Omega + \sum_{i=1}^{N} \kappa_i U_i \int_{\partial B_i} v\, dS \quad \forall v \in H_0^1(\Omega). \tag{4.1}$$

Proceeding as in [35] [Theorem 4.12] and Theorem 3.1, one can prove that problems (3.1) and (4.1) admit unique solutions $u_{\text{ref}} \in V(\Omega_p)$, and $u_{\text{int}} \in H_0^1(\Omega)$, respectively. We define the modelling error as $e := u_{\text{ref}} - u_{\text{red}}|_{\Omega_p}$, and we naturally decompose it as the error related to assumption (A1), that is $e_1 := u_{\text{ref}} - u_{\text{int}}|_{\Omega_p}$ and the one associated to (ii), namely $e_2 := u_{\text{int}} - u_{\text{red}}$. The two parts of the error are analysed separately, and we show that the following inequality holds true:

$$\begin{aligned}\|e\|_{H^1(\Omega_p)} &\leq \|e_1\|_{H^1(\Omega_p)} + \|e_2\|_{H^1(\Omega)} \\ &\leq C_1 \left[\|\mathcal{F}\|_{L^2(\Omega)} \sum_{i=1}^{N} R_i \left|\ln R_i\right|^{\frac{1}{2}} (1+\kappa_i) + \sum_{i=1}^{N} U_i \kappa_i R_i \left|\ln R_i\right|^{\frac{1}{2}} \right] \\ &\quad + C_2 \left[\|\mathcal{F}\|_{L^2(\Omega)} \sum_{i=1}^{N} \kappa_i R_i + \sum_{i,j=1}^{N} \kappa_i \kappa_j R_i R_j \left|\ln R_j\right|^{\frac{1}{2}} U_j \right], \end{aligned} \tag{4.2}$$

where the constants C_1 and C_2 are independent of R_i, κ_i and U_i, $\forall i \in \{1, \ldots, N\}$. Equation (4.2) informs us of the structure of the modelling error. The first two terms on the right hand side relate to the modelling assumption (A1) concerning extension of the physical domain Ω_p to the whole domain Ω. This component of the error scales quasi-linearly with the size of the inclusions. The third and fourth components on the right-hand side quantify the error of replacing the solution on the interfaces with its average and relate to the modelling assumption (A2). Since a modelling error for one interface affects all the other interfaces, not surprisingly the fourth term is proportional to $\sum_{i,j=1}^{N} R_i R_j$, up to a log-term.

4.1. *Analysis of the modelling error related to assumption (A1)*

In this subsection, we derive an upper bound depending on the parameters which occur in our model problem for the modelling error corresponding to assumption (A1). As a first step we define an elliptic auxiliary problem:

$$-\Delta u_{\text{f}} = \mathcal{F} \ \text{ in } \ \Omega, \ u_{\text{f}} = 0 \ \text{ on } \ \partial\Omega.$$

having the weak formulation:

$$(\nabla u_{\text{f}}, \nabla v)_{\Omega} = (\mathcal{F}, v)_{\Omega}, \ \forall v \in H_0^1(\Omega). \tag{4.3}$$

By means of the solution u_{f}, we decompose the solutions of (3.1) and (4.1) as follows:

$$u_{\text{ref}} = w_{\text{ref}} + u_{\text{f}}|_{\Omega_p} \ \text{ and } u_{\text{int}} = w_{\text{int}} + u_{\text{f}}. \tag{4.4}$$

Next, we introduce two extension operators

$$E_{\text{sa}} : V(\Omega_p) \to H_0^1(\Omega) \ \text{ and } E_{\text{st}} : H^2(\Omega) \to H_0^2\left(\hat{\Omega}\right)$$

presented in [30] [Section 2.1] and [13] [Theorem 7.25], respectively. Here, $\hat{\Omega}$ is an open and bounded set with $\Omega \Subset \hat{\Omega} \subset \mathbb{R}^2$. In order to derive a stability estimate for w_{ref}, we exploit the following properties of E_{sa} and E_{st}:

(P1) Let $v \in V(\Omega_p)$ then it holds: $E_{\mathrm{sa}} v|_{\Omega_p} = v$ and $\overline{E_{\mathrm{sa}} v}^{(i)} = \overline{v}^{(i)}$.

(P2) According to the proofs of [30] [Lemma 2.2, Theorem 2.2, Example 2.1], there is a constant $C_{\mathrm{sa}} > 0$ independent of R_i, such that:

$$\|\nabla E_{\mathrm{sa}} v\|_{L^2(\Omega)} \leq C_{\mathrm{sa}} \|\nabla v\|_{L^2(\Omega_p)} \text{ for } v \in V(\Omega_p).$$

(P3) For $v \in H^2(\Omega)$, there is a constant $C_{\mathrm{st}} > 0$, such that:

$$\|E_{\mathrm{st}} v\|_{H^2(\hat{\Omega})} \leq C_{\mathrm{st}} \|v\|_{H^2(\Omega)} \text{ and } E_{\mathrm{st}} v|_{\Omega} = v.$$

For $v = w_{\mathrm{ref}} \in V(\Omega_p)$ in (3.1), using the decomposition in (4.4) we obtain:

$$\begin{aligned}\|\nabla w_{\mathrm{ref}}\|^2_{L^2(\Omega_p)} \leq (\mathcal{F}, E_{\mathrm{sa}} w_{\mathrm{ref}})_{\Omega} - (\nabla u_{\mathrm{f}}, \nabla E_{\mathrm{sa}} w_{\mathrm{ref}})_{\Omega} - \sum_{i=1}^{N} (f_i, E_{\mathrm{sa}} w_{\mathrm{ref}})_{B_i} \\ + \sum_{i=1}^{N} (\nabla u_{\mathrm{f}}, \nabla E_{\mathrm{sa}} w_{\mathrm{ref}})_{B_i} - \sum_{i=1}^{N} \kappa_i (u_{\mathrm{f}}, w_{\mathrm{ref}})_{\partial B_i} + \sum_{i=1}^{N} U_i \kappa_i \int_{\partial B_i} w_{\mathrm{ref}} \, dS.\end{aligned}$$

Testing (4.3) with $v = E_{\mathrm{sa}} w_{\mathrm{ref}} \in H^1_0(\Omega)$, we have:

$$(\mathcal{F}, E_{\mathrm{sa}} w_{\mathrm{ref}})_{\Omega} - (\nabla u_{\mathrm{f}}, \nabla E_{\mathrm{sa}} w_{\mathrm{ref}})_{\Omega} = 0$$

and by (P1) and the Hölder inequality, it follows:

$$\begin{aligned}\|\nabla w_{\mathrm{ref}}\|^2_{L^2(\Omega_p)} \leq \sum_{i=1}^{N} \|f_i\|_{L^2(B_i)} \|E_{\mathrm{sa}} w_{\mathrm{ref}}\|_{L^2(B_i)} + \sum_{i=1}^{N} \|\nabla u_{\mathrm{f}}\|_{L^2(B_i)} \|\nabla E_{\mathrm{sa}} w_{\mathrm{ref}}\|_{L^2(B_i)} \\ + \sum_{i=1}^{N} \kappa_i \|u_{\mathrm{f}}\|_{L^2(\partial B_i)} \|w_{\mathrm{ref}}\|_{L^2(\partial B_i)} + 2\pi \sum_{i=1}^{N} U_i \kappa_i R_i \cdot \overline{w}^{(i)}_{\mathrm{ref}}.\end{aligned}$$

In order to bound the first summand, we consider once again the Hölder inequality with the parameters r and s fulfilling the condition $1/r + 1/s = 1$. By means of this, one can show that:

$$\|E_{\mathrm{sa}} w_{\mathrm{ref}}\|_{L^2(B_i)} \leq C R_i^{\frac{1}{r}} \|E_{\mathrm{sa}} w_{\mathrm{ref}}\|_{L^{2s}(B_i)} \tag{4.5}$$

Setting $s = p/2$ and using (2.1), we obtain:

$$\|E_{\mathrm{sa}} w_{\mathrm{ref}}\|_{L^2(B_i)} \leq C R_i^{1-\frac{2}{p}} p^{\frac{1}{2}} \|\nabla E_{\mathrm{sa}} w_{\mathrm{ref}}\|_{L^2(\Omega)}. \tag{4.6}$$

Then it follows for $p = |\ln R_i|$ together with (1.7) and (P2):

$$\sum_{i=1}^{N} \|f_i\|_{L^2(B_i)} \|E_{\mathrm{sa}} w_{\mathrm{ref}}\|_{L^2(B_i)} \leq C \|\mathcal{F}\|_{L^2(\Omega)} \|\nabla w_{\mathrm{ref}}\|_{L^2(\Omega_p)} \sum_{i=1}^{N} R_i |\ln R_i|^{\frac{1}{2}}. \tag{4.7}$$

Analogously to (4.5) and (4.6) one can show that:

$$\|\nabla u_{\mathrm{f}}\|_{L^2(B_i)} \leq C R_i^{1-\frac{2}{p}} \|\nabla u_{\mathrm{f}}\|_{L^p(B_i)}.$$

Based on (2.1), (P3) and the H^2-regularity of u_f, we obtain:

$$\begin{aligned}\|\nabla u_\mathrm{f}\|_{L^p(B_i)} &\leq \left(\sum_{i=1}^{2} \|\partial_{x_i} E_\mathrm{st} u_\mathrm{f}\|^p_{L^p(\hat{\Omega})}\right)^{1/p} \leq C p^{\frac{1}{2}} \left(\sum_{i=1}^{2} \|\nabla\left(\partial_{x_i} E_\mathrm{st} u_\mathrm{f}\right)\|^p_{L^2(\hat{\Omega})}\right)^{1/p} \\ &\leq C p^{\frac{1}{2}} \|E_\mathrm{st} u_\mathrm{f}\|_{H^2(\hat{\Omega})} \leq C p^{\frac{1}{2}} \|u_\mathrm{f}\|_{H^2(\Omega)} \leq C p^{\frac{1}{2}} \|\mathcal{F}\|_{L^2(\Omega)}\,.\end{aligned}$$

Choosing $p = |\ln R_i|$ the following estimate for the second summand results in:

$$\sum_{i=1}^{N} \|\nabla u_\mathrm{f}\|_{L^2(B_i)} \|\nabla E_\mathrm{sa} w_\mathrm{ref}\|_{L^2(B_i)} \leq C \|\mathcal{F}\|_{L^2(\Omega)} \|\nabla w_\mathrm{ref}\|_{L^2(\Omega_p)} \sum_{i=1}^{N} R_i \left|\ln R_i\right|^{\frac{1}{2}}. \tag{4.8}$$

Applying Lemma 2.2, (P1) and (P2) to the third summand and considering the H^2-regularity of u_f together with a standard Sobolev embedding, we have:

$$\sum_{i=1}^{N} \kappa_i \|u_\mathrm{f}\|_{L^2(\partial B_i)} \|w_\mathrm{ref}\|_{L^2(\partial B_i)} \leq C \|\mathcal{F}\|_{L^2(\Omega)} \|\nabla w_\mathrm{ref}\|_{L^2(\Omega_p)} \sum_{i=1}^{N} \kappa_i R_i \left|\ln R_i\right|^{\frac{1}{2}}. \tag{4.9}$$

The bound for the last summand follows directly from Lemma 2.1 and (P3):

$$2\pi \sum_{i=1}^{N} U_i \kappa_i R_i \cdot \overline{w}^{(i)}_\mathrm{ref} \leq C \|\nabla w_\mathrm{ref}\|_{L^2(\Omega_p)} \sum_{i=1}^{N} U_i \kappa_i R_i \left|\ln R_i\right|^{\frac{1}{2}}. \tag{4.10}$$

Summarizing (4.7)-(4.10), we finally have:

$$\|\nabla w_\mathrm{ref}\|_{L^2(\Omega_p)} \leq C \left[\|\mathcal{F}\|_{L^2(\Omega)} \sum_{i=1}^{N} R_i \left|\ln R_i\right|^{\frac{1}{2}} (1+\kappa_i) + \sum_{i=1}^{N} U_i \kappa_i R_i \left|\ln R_i\right|^{\frac{1}{2}}\right]. \tag{4.11}$$

As a next step, we derive a stability estimate for the function w_int. In this process, (4.1) is tested with $v = w_\mathrm{int} \in H^1_0(\Omega)$. Inserting the decomposition of u_int (see (4.4)) into (4.1), it follows that

$$\begin{aligned}\|\nabla w_\mathrm{int}\|^2_{L^2(\Omega)} \leq (\mathcal{F}, w_\mathrm{int})_\Omega - (\nabla u_\mathrm{f}, \nabla w_\mathrm{int})_\Omega - \sum_{i=1}^{N} \kappa_i \left(u_\mathrm{f}, w_\mathrm{int}\right)_{L^2(\partial B_i)} \\ + 2\pi \sum_{i=1}^{N} U_i \kappa_i R_i \cdot \overline{w}^{(i)}_\mathrm{int}.\end{aligned}$$

By means of the techniques which have been used to derive the stability estimate for w_ref one can prove that:

$$\|\nabla w_\mathrm{int}\|_{L^2(\Omega)} \leq C \left[\|\mathcal{F}\|_{L^2(\Omega)} \sum_{i=1}^{N} \kappa_i R_i \left|\ln R_i\right|^{\frac{1}{2}} + \sum_{i=1}^{N} U_i \kappa_i R_i \left|\ln R_i\right|^{\frac{1}{2}}\right]. \tag{4.12}$$

Based on (4.11) and (4.12) an upper bound for the error component e_1 can be derived:

$$\begin{aligned}\|e_1\|_{H^1(\Omega_p)} &= \|w_{\rm ref} - w_{\rm int}\|_{H^1(\Omega_p)} \leq \|w_{\rm ref}\|_{H^1(\Omega_p)} + \|w_{\rm int}\|_{H^1_0(\Omega)} \\ &\leq \|E_{\rm sa} w_{\rm ref}\|_{H^1_0(\Omega)} + \|w_{\rm int}\|_{H^1_0(\Omega)} \leq C\left(\|\nabla w_{\rm ref}\|_{L^2(\Omega_p)} + \|\nabla w_{\rm int}\|_{L^2(\Omega)}\right) \\ &\leq C_1\left[\|\mathcal{F}\|_{L^2(\Omega)} \sum_{i=1}^{N} R_i \left|\ln R_i\right|^{\frac{1}{2}} (1+\kappa_i) + \sum_{i=1}^{N} U_i \kappa_i R_i \left|\ln R_i\right|^{\frac{1}{2}}\right].\end{aligned}$$

4.2. *Analysis of the modelling error related to assumption (A2)*

Here, we aim to derive an upper bound for e_2, in terms of the data and the geometrical configuration of the inclusions. By subtracting problem (3.3) from (4.1) and rearranging the terms, we obtain the following equation:

$$\begin{aligned}(\nabla(u_{\rm int} - u_{\rm red}), \nabla v)_\Omega + \sum_{i=1}^{N} \kappa_i (u_{\rm int} - u_{\rm red}, v)_{\partial B_i} \\ + \sum_{i=1}^{N} \kappa_i (u_{\rm red} - \overline{u}^{(i)}_{\rm red}, v)_{\partial B_i} = 0, \quad \forall v \in H^1_0(\Omega)\,.\end{aligned}$$

Recalling that $\widetilde{u}^{(i)}_{\rm red} = u_{\rm red} - \overline{u}^{(i)}_{\rm red}$ and choosing $v = e_2 = u_{\rm int} - u_{\rm red} \in H^1_0(\Omega)$ it follows:

$$\|\nabla e_2\|^2_{L^2(\Omega)} \leq \sum_{i=1}^{N} \kappa_i \left(-\widetilde{u}^{(i)}_{\rm red}, e_2\right)_{\partial B_i} \leq \sum_{i=1}^{N} \kappa_i \|\widetilde{u}^{(i)}_{\rm red}\|_{L^2(\partial B_i)} \|e_2 - \overline{e}^{(i)}_2\|_{L^2(\partial B_i)}.$$

This intermediate result is coherent with assumption (A2), because it shows that if the fluctuations on the interfaces ∂B_i are small, then the modelling error is small too. Now by Lemma (2.2) and the stability estimate in Theorem 3.1, we have:

$$\begin{aligned}\|\nabla e_2\|^2_{L^2(\Omega)} &\leq \sum_{i=1}^{N} \kappa_i R_i \|\nabla u_{\rm red}\|_{L^2(\Omega)} \|\nabla e_2\|_{L^2(\Omega)} \\ &\leq C_2\left[\|\mathcal{F}\|_{L^2(\Omega)} \sum_{i=1}^{N} \kappa_i R_i + \sum_{i,j=1}^{N} \kappa_i \kappa_j R_i R_j |\ln R_j|^{\frac{1}{2}} U_j\right] \|\nabla e_2\|_{L^2(\Omega)}.\end{aligned}$$

By means of Poincaré's inequality, the result reported in inequality (4.2) is proved.

5. Numerical approximation

In this section, we study the convergence behaviour of a standard finite element discretization applied to the variational problem (3.4). Let $\mathcal{T}_h$ be a family of quasi-uniform triangular meshes which partitions the computational domain Ω. By h, we

denote the characteristic mesh size of the grid. As a finite element space $V_h \subset H_0^1(\Omega)$ piecewise linear finite elements are considered:

$$V_h = \left\{ v \in C\left(\overline{\Omega}\right) \cap H_0^1(\Omega) \,\middle|\, v|_T \in \mathbb{P}^1(T),\ T \in \mathcal{T}_h \right\},$$

where $\mathbb{P}^1(T)$ is the vector space of first order polynomials defined on T. Using the notation from Section 3, the numerical solution $u_h \in V_h$ has to fulfill the following equation:

$$a(u_{h,\mathrm{red}}, v_h) = L(v_h), \quad \forall v_h \in V_h. \tag{5.1}$$

A first convergence result for this discretization is provided in the next theorem.

Theorem 5.1. *Let $u_{\mathrm{red}} \in H_0^1(\Omega) \cap H^{\frac{3}{2}-\epsilon}(\Omega)$ be the solution of (3.4) and let $u_{h,\mathrm{red}}$ be defined by (5.1). For the discretization error $u_{\mathrm{red}} - u_{h,\mathrm{red}}$, we have the upper bounds*

$$\|u_{\mathrm{red}} - u_{h,\mathrm{red}}\|_{H^1(\Omega)} \leq C_1 h^{\frac{1}{2}-\epsilon} \|u_{\mathrm{red}}\|_{H^{\frac{3}{2}-\epsilon}(\Omega)}$$

and

$$\|u_{\mathrm{red}} - u_{h,\mathrm{red}}\|_{L^2(\Omega)} \leq C_2 h^{\frac{3}{2}-\epsilon} \|u_{\mathrm{red}}\|_{H^{\frac{3}{2}-\epsilon}(\Omega)}$$

for $0 < \epsilon \leq \frac{1}{2}$ and some constants C_1, C_2 independent of h.

Proof. It is obvious that the linear form L and the bilinear form a in (3.5) and (3.6) fulfill all the conditions for Céa's lemma (see proof of Theorem 3.1). Therefore the H^1-error can be bounded by an interpolation error:

$$\|u_{\mathrm{red}} - u_{h,\mathrm{red}}\|_{H^1(\Omega)} \leq \sqrt{\frac{C_a}{\alpha}} \|u_{\mathrm{red}} - S_h u_{\mathrm{red}}\|_{H^1(\Omega)}, \tag{5.2}$$

where $S_h : H^1(\Omega) \to V_h$ is a suitable interpolation operator. C_a and α denote the continuity and ellipticity constant of the bilinear form a. Choosing for S_h the Scott-Zhang operator [33] [Theorem 4.1] and considering the regularity result in Theorem 3.1, the first estimate follows. Please note that from the proof of Theorem 3.1 it can be concluded that the constant in (5.2) is bounded, even if R_i tends to zero. Based on the first estimate, the second estimate can be shown by means of an Aubin-Nitsche argument. □

We note that although the solution is not globally in H^2, and thus we cannot expect $\mathcal{O}(h)$ convergence in the H^1-norm, the solution restricted to Ω_p and Ω_f can be expected to be in H^2. Therefore we can apply particular techniques to improve the accuracy of the numerical approximation. In this work, we discuss two possibilities to bypass the reduced regularity of the solution by modifying the computational grid. The modification of the grid consists in adapting the grid to the interfaces $\partial B_j,\ j \in \{1, \ldots, N\}$ such that optimal error estimates can be derived. In the literature they are refered to as δ-resolving [24] (Definition 3.1) and graded meshes

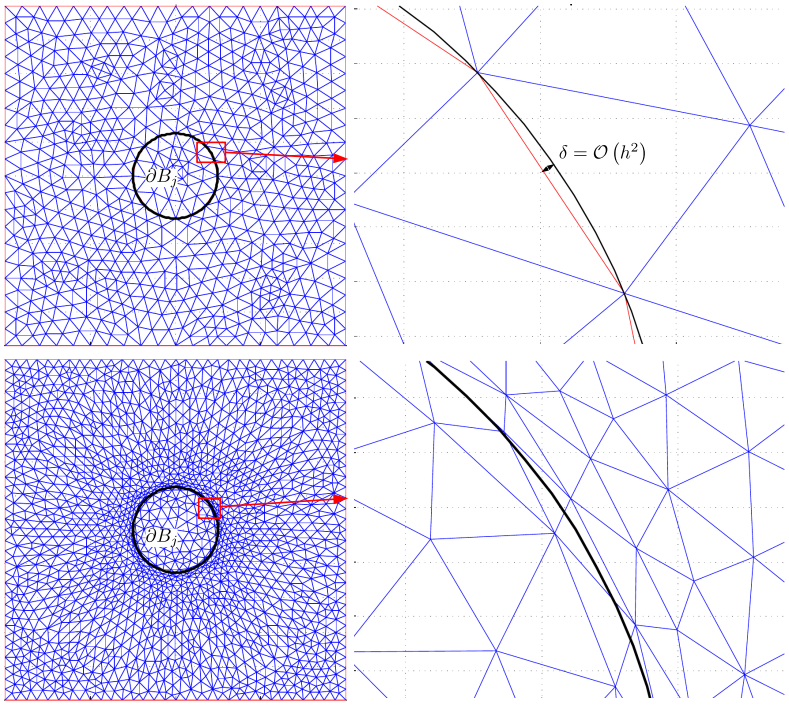

Fig. 1. Adapted meshes for a circular interface ∂B_j: δ-resolving mesh with $\delta = \mathcal{O}\left(h^2\right)$ (top), graded mesh (bottom).

[6] (Section 3.1). Other ways to handle the lower regularity employ, e.g., appropriate error norms [19], or an appropriate finite element space [11].

A grid $\mathcal{T}_h$ is δ-resolving with respect to an interface ∂B_j, if the boundaries of the subgrids corresponding to B_j and $\Omega \setminus B_j$ have a maximal distance of δ to the interface ∂B_j. In this work, we consider a special type of a δ-resolving grid, in which the element edges adjacent to ∂B_j form an interpolating linear spline for this interface (see Figure 1, top). From standard interpolation theory, it is well known that in this case $\delta = \mathcal{O}\left(h^2\right)$ holds. Note that to fulfill this property, $\mathcal{T}_h$ does not have to be refined locally.

Contrary to that, a grid that is graded with respect to ∂B_j exhibits local refinements along ∂B_j, since a graded mesh has the feature that the diameters of the elements are scaled by the distance to the interface, such that the element diameters become smaller the nearer they are located to the interface [2][Section 2] (see Figure 1, bottom). Let us denote the minumum distance of an element T to the interfaces ∂B_j by r_T and the diameter of T by h_T. For the purpose of this work, it is sufficient to consider a particular case of the graded meshes presented in [6][Section 3.1]. For a characteristic mesh size h, we assume that the local element size h_T scales as $\sqrt{r_T}$ and that $h_T \approx h^2$ if T is close to ∂B_i. In other words, let $\delta > 0$ be a fixed coefficient

(e.g., $\delta = \frac{1}{2}$), then we assume

$$h_T \approx \begin{cases} h\sqrt{r_T}, & \text{if } r_T > \delta h_T, \\ h^2, & \text{otherwise.} \end{cases} \tag{5.3}$$

In the next theorem, we show that using a δ-resolving or a graded mesh, optimal convergence rates can be recovered, provided that the corresponding solution exhibits some local smoothness.

Theorem 5.2. *Let u be the weak solution of (3.4) such that it holds: $u_{\mathrm{red}} \in H^2(\Omega_s)$, where $\Omega_s = \Omega_p \cup \Omega_f$ (see (1.1)). By $\mathcal{T}_h^\delta$ we denote a family of δ-resolving meshes with $\delta = \mathcal{O}(h^2)$ and by $\mathcal{T}_h^g$ we denote a family of graded meshes. Both meshes are adapted to the interfaces ∂B_j, $j \in \{1, \dots, N\}$. The corresponding finite element solutions of (5.1) are u_h^δ and u_h^g. On these condtions, one can prove for the discretization errors $u_{\mathrm{red}} - u_{h,\mathrm{red}}^k$, $k \in \{\delta, g\}$ the following optimal $H^1(\Omega)$- and $L^2(\Omega)$-estimates:*

(E1) $\|u_{\mathrm{red}} - u_{h,\mathrm{red}}^\delta\|_{H^1(\Omega)} + \dfrac{1}{h}\|u_{\mathrm{red}} - u_{h,\mathrm{red}}^\delta\|_{L^2(\Omega)} \lesssim h\|u_{\mathrm{red}}\|_{H^2(\Omega_s)}$,

(E2) $\|u_{\mathrm{red}} - u_{h,\mathrm{red}}^g\|_{H^1(\Omega)} + \dfrac{1}{h}\|u_{\mathrm{red}} - u_{h,\mathrm{red}}^g\|_{L^2(\Omega)} \lesssim h^{1-\epsilon}\|u_{\mathrm{red}}\|_{H^{\frac{3}{2}-\epsilon}(\Omega)} + h\,\|u_{\mathrm{red}}\|_{H^2(\Omega_s)}$,

where $0 < \epsilon \leq \frac{1}{2}$.

Proof. As in the proof of the previous theorem, the H^1-errors for both discretizations can be bounded by an interpolation error. In the case of the δ-resolving mesh, we use a modified Clément operator S_{ch} presented in [24] [Definition 3.3]. For this operator one can prove the following approximation result [24] [Theorem 3.5]:

$$\|u_{\mathrm{red}} - S_{ch}u_{\mathrm{red}}\|_{H^1(\Omega)}^2 \lesssim h^2\,\|u_{\mathrm{red}}\|_{H^2(\Omega_s)}^2 + \delta\,\|u_{\mathrm{red}}\|_{H^2(\Omega_s)}^2. \tag{5.4}$$

Then estimate (E1) follows from the assumption $\delta = \mathcal{O}(h^2)$. For a graded mesh $\mathcal{T}_h^g$, we choose the Scott-Zhang operator S_{zh} from [33] [Theorem 4.1] and compute:

$$\begin{aligned}\|u_{\mathrm{red}} - S_{zh}u_{\mathrm{red}}\|_{H^1(\Omega)}^2 &= \sum_{T\in\mathcal{T}_h^g} \|u_{\mathrm{red}} - S_{zh}u_{\mathrm{red}}\|_{H^1(T)}^2 \\ &= \sum_{\substack{T\in\mathcal{T}_h^g \\ r_T \leq \delta h_T}} \|u_{\mathrm{red}} - S_{zh}u_{\mathrm{red}}\|_{H^1(T)}^2 + \sum_{\substack{T\in\mathcal{T}_h^g \\ r_T > \delta h_T}} \|u_{\mathrm{red}} - S_{zh}u_{\mathrm{red}}\|_{H^1(T)}^2\end{aligned}$$

By Theorem 3.1 for the elements of the first summand we have :

$$\|u_{\mathrm{red}} - S_{zh}u_{\mathrm{red}}\|_{H^1(T)}^2 \lesssim h_T^{1-2\epsilon}\,\|u_{\mathrm{red}}\|_{H^{\frac{3}{2}-\epsilon}(\omega_T)}^2,$$

where ω_T is a patch of elements around T. For $0 < \epsilon \leq \frac{1}{2}$ and using (5.3), we have:

$$\sum_{\substack{T\in\mathcal{T}_h^g \\ r_T \leq \delta h_T}} \|u_{\mathrm{red}} - S_{zh}u_{\mathrm{red}}\|_{H^1(T)}^2 \lesssim h^{2-4\epsilon}\,\|u_{\mathrm{red}}\|_{H^{\frac{3}{2}-\epsilon}(\Omega)}^2. \tag{5.5}$$

Using $u_{\text{red}} \in H^2(\Omega_s)$ and the approximation properties of S_{zh}, for the second summand we have:

$$\sum_{\substack{T\in\mathcal{T}_h^g \\ r_T>\delta h_T}} \|u_{\text{red}} - S_{zh}u_{\text{red}}\|^2_{H^1(T)} \lesssim h^2 \|u_{\text{red}}\|^2_{H^2(\Omega_s)}. \tag{5.6}$$

Combing (5.5) and (5.6), we obtain the H^1-estimate. The L^2-estimates follow from an Aubin-Nitsche argument. □

6. Numerical experiments

The objective of this section is to support by means of numerical evidence the theoretical results of Section 4 and 5. In the first subsection, we show to what extent the solutions of problem (3.1) and of the simplified model (3.3) differ. The second subsection contains several tests addressing the convergence results in Theorem 5.1 and 5.2.

6.1. *Investigation of the modelling error*

In this subsection, we analyse numerically the modelling error in (4.2). Let us consider a single source term, that is, we set $N = 1$ in (1.3). We denote with u_{ref} and u_{red} the analytical solutions to problem (3.1) and (3.3), respectively. In the general case, these solutions are not known a priori. Therefore, we verify (4.2) using their linear finite element approximations $u_{h,\text{ref}}$ and $u_{h,\text{red}}$, respectively, since the numerical solutions converge to the corresponding analytical solutions as the mesh size goes to zero. We define the reduced problem (3.3) on the domain $\Omega = (-1, 1)^2$, while the full dimensional problem (3.1) is posed on $\Omega_p = \Omega\setminus B_1$, where the only circular inclusion B_1 is a ball of radius R with centre in $(0.3, 0.4)$. In many applications, the radius of the inclusion is the most relevant parameter and with estimate (4.2) we have proved that the error introduced adopting the reduced model tends to zero as the radius of the inclusion becomes smaller. Therefore, in this test, we analyse the influence of the size of the inclusion, that is, we vary its radius R, while keeping the other parameters constant. In order to verify the dependency of the modelling error on the radius R of the inclusion, we take $R \in \{0.1, 0.05, 0.025, 0.0125, 0.00625, 0.003125\}$, while we set $\kappa = U = 1$ constant for all simulations. As the source term, we choose the function

$$\mathcal{F}(x, y) = \sin(9x) + \sin(13y) + x + y, \qquad \text{for } (x, y) \in \Omega.$$

According to Theorem 5.1 and standard convergence results, we can bound the modelling error by:

$$\begin{aligned}\|u_{\text{ref}} - u_{\text{red}}\|_{H^1(\Omega_p)} &\le \|u_{\text{ref}} - u_{h,\text{ref}}\|_{H^1(\Omega_p)} + \|u_{\text{red}} - u_{h,\text{red}}\|_{H^1(\Omega_p)} \\ &\quad + \|u_{h,\text{ref}} - u_{h,\text{red}}\|_{H^1(\Omega_p)} \\ &\lesssim \mathcal{O}\left(h^{\frac{1}{2}}\right) + \|u_{h,\text{ref}} - u_{h,\text{red}}\|_{H^1(\Omega_p)}.\end{aligned}$$

As the mesh size h tends to zero, we may assume that the modelling error between numerical solutions converges to the actual modelling error, as Fig. 2 suggests. As an error measure, we employ the numerical modelling error defined by:

$$\mathrm{err} = \|u_{h,\mathrm{ref}} - u_{h,\mathrm{red}}\|_{H^1(\Omega_p)}.$$

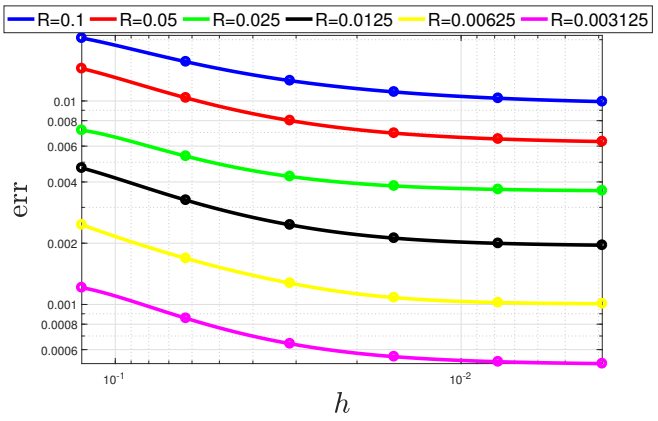

Fig. 2. The numerical modelling error is calculated for different values of the mesh characteristic size ($h = 2^{-i}$ for $i = 3, ..., 7$) and for different radii of the ball B_1 (each line shown with different colors). For each radius the modeling error values are interpolated using splines. We observe that as the mesh size h tends to zero, the error converges to a fixed value, which is the actual modelling error.

Furthermore, we define an error functional to show the experimental order of convergence by

$$\mathrm{Rate} = \frac{\log(\mathrm{err}(R_1)/\mathrm{err}(R_2))}{\log(R_1/R_2)},$$

where $err(R)$ is the numerical modelling error for the radius R. In Table 1, the modelling error, computed at the finest level of the δ-resolving mesh, is provided for different radii together with the rate of convergence with respect to the radius R of the inclusion. We observe that the modelling error decays quasi-linearly as R, which is in good agreement with our estimate (4.2).

6.2. *Convergence tests*

The objective of this section is to illustrate the convergence results of of Theorems 5.1 and 5.2 by means of numerical experiments based on test cases where the analytical solution is explicitly available. For our first convergence test, we consider a single source term, i.e., we set in (1.3) $N = 1$. The ball B_1 has the radius $R = 0.25$ and the centre $x_1 = (0, 0)$. As a computational domain, we choose the square:

Table 1. The numerical modelling error is shown for different radii and $\kappa = U = 1$. The convergence rate is reported in the last column.

R	err	Rate
0.1	$9.92770e-03$	/
0.05	$6.31752e-03$	0.65
0.025	$3.62451e-03$	0.80
0.0125	$1.95587e-03$	0.89
0.00625	$1.00884e-03$	0.96
0.003125	$5.12174e-04$	0.98

$\Omega = (-1,1)^2 \subset \mathbb{R}^2$. The remaining parameters of the problem are given by $\kappa_1 = 0.1$ and $U_1 = 1$. Setting $\mathcal{F} \equiv 0$ and appropriate Dirichlet boundary conditions, the exact solution of this problem is given by [8]:

$$u_{e,1}(x) = \begin{cases} U_1 \frac{\kappa_1}{1+\kappa_1} \left(1 - R \ln\left(\frac{r}{R}(x)\right)\right), & r(x) > R, \\ U_1 \frac{\kappa_1}{1+\kappa_1}, & r(x) \leq R, \end{cases}$$

where $r(x)$ is the Euclidean distance from an arbitrary point $x \in \Omega$ to the centre of the ball B_1:

$$r(x) = \|x - x_1\|_2 . \tag{6.1}$$

The numerical solution $u_{h,1}$ is defined by (5.1), and the numerical discretization

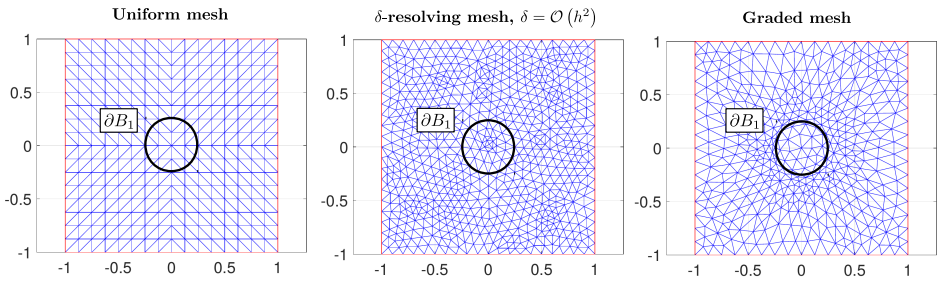

Fig. 3. Three different types of meshes are used for the first convergence test (single point source term). left: Uniform mesh (521 elements), middle: δ-resolving mesh, $\delta = \mathcal{O}(h^2)$ (1368 elements), right: Graded mesh (870 elements).

error $e_{h,1}$ is given as follows: $e_{h,1} = u_{e,1} - u_{h,1}$. For the triangulation of Ω three different types of meshes are used: A uniform mesh, a δ-resolving mesh with $\delta = \mathcal{O}(h^2)$ and a graded mesh, defined by (5.3). The second refinement levels of these grid types are depicted in Fig. 3. Tables 2 and 3 show the discretization errors $e_{h,1}$ with respect to the L^2- and the H^1-norm. Considering the convergence rates in

both tables it can be seen that the theoretical convergence results in Theorem 5.1 and 5.2 are confirmed, since it holds $u_{e,1} \in H^2(\Omega_s)$.

Table 2. L^2-norms of $e_{h,1}$ and convergence rates for three different meshes (uniform, δ-resolving, graded). In the last line of the table the theoretical convergence rates are listed.

Level	uniform mesh	Rate	δ-resolving mesh	Rate	graded mesh	Rate
1	$8.506954e-03$	/	$8.844852e-04$	/	$1.154294e-03$	/
2	$2.717929e-03$	1.65	$2.272761e-04$	1.96	$2.517585e-04$	2.20
3	$8.675497e-04$	1.65	$4.925913e-05$	2.21	$7.779338e-05$	1.69
4	$3.011329e-04$	1.53	$1.452474e-05$	1.76	$2.061325e-05$	1.92
5	$1.041544e-04$	1.53	$3.649972e-06$	1.99	$4.491752e-05$	2.20
	expected:	**1.50**	expected:	**2.00**	expected:	**2.00**

Table 3. H^1-norms of $e_{h,1}$ and convergence rates for three different meshes (uniform, δ-resolving, graded). In the last line of the table the theoretical convergence rates are listed.

Level	uniform mesh	Rate	δ-resolving mesh	Rate	graded mesh	Rate
1	$6.074554e-02$	/	$2.463609e-02$	/	$2.826352e-02$	/
2	$3.995154e-02$	0.60	$1.132668e-02$	1.12	$1.482623e-02$	0.93
3	$2.995280e-02$	0.42	$5.583932e-03$	1.02	$9.268436e-03$	0.68
4	$2.047021e-02$	0.55	$2.772943e-03$	1.01	$4.954802e-03$	0.90
5	$1.460174e-02$	0.49	$1.381250e-03$	1.01	$2.162039e-03$	1.20
	expected:	**0.50**	expected:	**1.00**	expected:	**1.00**

As a next step we want to study problem (1.3) with several circular inclusions B_i for $i = 1, ..., N$ $(N > 1)$. For this purpose, a new analytical solution $u_{e,2}$ is determined. Analogously to (6.1), the distance between the centres of the balls x_i and an arbitrary point $x \in \Omega$ is given by $r_i(x) = \|x - x_i\|_2$, $i \in \{1, \dots, N\}$. Using this notation we define the solution $u_{e,2}$ as a linear combination:

$$u_{e,2}(x) = \begin{cases} \sum_{i=1}^{N} \alpha_i \left(1 - R_i \log \frac{r_i}{R_i}\right), & x \notin \bigcup_{i=1}^{N} B_i, \\ G_i(x), & x \in B_i, \end{cases}$$

where $\alpha_i \in \mathbb{R}$ and $G_i(x)$ is a harmonic function in B_i. Then it holds:

$$-\Delta u_{e,2} = \sum_{i=1}^{N} \alpha_i \delta_{\partial B_i}. \tag{6.2}$$

A comparison of the right hand sides in (6.2) and (1.3) yields the following equations for the coefficients α_i:

$$\alpha_i = \kappa_i \left(U_i - \overline{u}_{e,2}^{(i)}\right), \ i \in \{1, \dots, N\}.$$

In order to compute the average $\overline{u}_{e,2}^{(i)}$, we use the fact that the functions

$$u_j = 1 - R_j \log \frac{r_j}{R_j},\ j \in \{1, \dots, N\} \setminus \{i\}$$

are harmonic in B_i. By the mean-value formula for harmonic functions [9] [Chapter 2.2, Theorem 2], we have:

$$\overline{u}_j^{(i)} = 1 - R_j \log \frac{r_{ij}}{R_j},\ r_{ij} = \|x_j - x_i\|_2\,,\ i \neq j,$$

resulting in the following expression for $\overline{u}_{e,2}^{(i)}$:

$$\overline{u}_{e,2}^{(i)} = \alpha_i + \sum_{j \neq i} \alpha_j \overline{u}_j^{(i)}.$$

Now, the coefficient vector $\alpha = (\alpha_1, \dots, \alpha_N)^T$ can be determined by a system of equations:

$$A \cdot \alpha = b,$$

where the matrix $A \in \mathbb{R}^{N \times N}$ and the right hand side $b \in \mathbb{R}^N$ are given by:

$$A_{ij} = (1 + \kappa_i)\,\delta_{ij} + \kappa_i \overline{u}_j^{(i)}\,(1 - \delta_{ij}) \quad \text{and} \quad b_i = \kappa_i U_i,\ i, j \in \{1, \dots, N\}\,.$$

It remains to determine the functions G_i on B_i. An appropriate expression for these functions is given by the following linear combination:

$$G_i = \alpha_i + \sum_{j \neq i} \alpha_j \left(1 - R_j \log \frac{r_j}{R_j}\right),$$

since these functions are harmonic and represent a continuous extension of $u_{e,2}|_{\Omega \setminus \bigcup_{i=1}^N B_i}$.

For the numerical simulations, we again consider $\Omega = (-1, 1)^2$ and 5 source terms ($N = 5$, Fig. 4). As in the case $N = 1$ the boundary conditions are adjusted such that $u_{e,2}$ is the exact solution of problem (1.3). Table 4 contains the remaining parameters used for the numerical simulations. The discretization errors in the L^2- and the H^1-norm summarized in Table 5 are based on a uniform triangulation of Ω (see e.g. Fig. 3, left). We observe that the discretization scheme converges as predicted by Theorem 5.1.

7. A 3D problem coupled with 1D inclusions with application to microcirculation

We present a prototype model for stationary flow in a permeable biological tissue perfused by a network of capillaries. Although flow in the capillary network is better described by a mixed type model addressing velocity and pressure simultaneously and transport of chemical species is often unsteady, we consider here steady coupled elliptic problems. The domain Ω where the model is composed of two parts, Ω_p and Ω_f, denoting the interstitial volume and the capillaries, respectively. We assume

Table 4. Parameter set used for problem (1.3) with $N = 5$ source terms.

	x_i	R_i	U_i	κ_i
B_1	$(-0.50, 0.50)$	0.15	2.30	0.12
B_2	$(0.75, -0.25)$	0.20	2.50	0.10
B_3	$(-0.50, 0.50)$	0.25	2.80	0.09
B_4	$(0.25, 0.25)$	0.10	2.50	0.08
B_5	$(0.25, -0.75)$	0.05	3.00	0.25

Table 5. L^2- and H^1-norms and of $e_{h,2}$. In the last line of the table the theoretical convergence rates are listed.

Level	L^2-error	Rate	H^1-error	Rate
1	$2.669615e-02$	/	$1.884496e-01$	/
2	$8.892418e-03$	1.59	$1.749503e-01$	0.11
3	$3.855905e-03$	1.21	$1.177106e-01$	0.57
4	$1.279445e-03$	1.59	$8.816140e-02$	0.42
5	$4.521436e-04$	1.50	$6.029469e-02$	0.55
6	$1.537090e-04$	1.56	$4.283918e-02$	0.50
	expected:	**1.50**	expected:	**0.50**

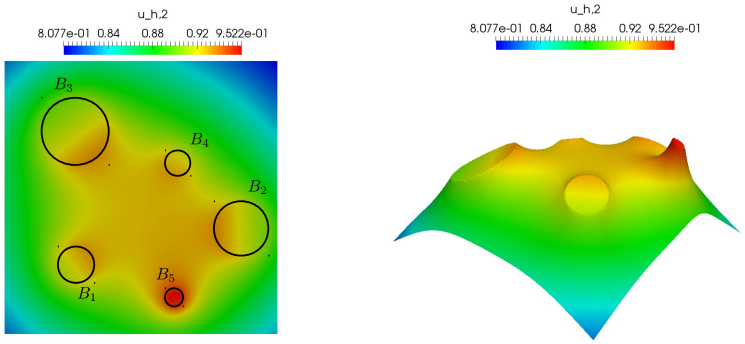

Fig. 4. Location of the balls $B_1, \ldots, B_5$ in the computational domain $\Omega = (-1, 1)^2$ (left), Three-dimensional graph of the numerical solution $u_{h,2}$ based on the parameters in Table 4 (right).

that the capillaries can be described as cylindrical vessels and Λ denotes their centre line. We decompose the network Λ into individual branches Λ_i. Branches are parametrized by the arc length s_i; a tangent unit vector $\boldsymbol{\lambda}_i$ is also defined over each branch, determining in this way an arbitrary branch orientation. The capillary radius R_i, is for simplicity considered to be constant along each branch of the network. In particular, the domain Ω_f can be split into cylindrical branches Ω_i

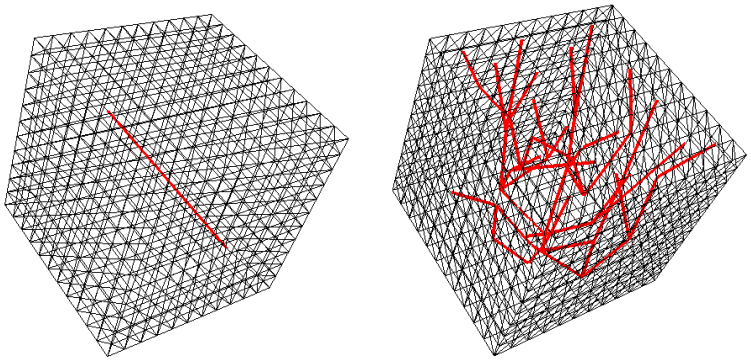

Fig. 5. Visualization of the domains Ω and Λ used in the idealized simulations of microcirculation. The computational mesh of Ω is also shown. We consider two distinct test cases: on the left the network consist of one single segment; on the right the network is a graph with 22 branches.

defined as follows:

$$\Omega_i = \{\boldsymbol{x} \in \mathbb{R}^3;\ \boldsymbol{x} = \boldsymbol{s} + \boldsymbol{r}\}, \boldsymbol{s} \in \Lambda_i = \mathcal{M}_i(\Lambda' \subset \mathbb{R}^1),$$
$$\boldsymbol{r} \in \mathcal{D}_{\Lambda_i}(R_i) = \{r\boldsymbol{n}_{\Lambda_i};\ r \in (0, R_i)\},$$

where $\mathcal{M}_i$ is a mapping from a reference domain Λ' to the manifold $\Lambda_i \subset \mathbb{R}^3$ and $\boldsymbol{n}_{\Lambda_i}$ denotes a unit normal vector with respect to Λ_i. We denote with Γ_i the lateral surface of Ω_i. Using this notation, problem (1.2) becomes,

$$\begin{cases} -\Delta u_p = 0 & \text{in } \Omega_p, \\ -\Delta u_f = 0 & \text{in } \Omega_f, \\ -\nabla u_p \cdot \mathbf{n}_p = \kappa_i \left(u_p - u_f\right) & \text{on } \Gamma_i, \\ -\nabla u_f \cdot \mathbf{n}_f = \kappa_i \left(u_f - u_p\right) & \text{on } \Gamma_i, \\ u_p = 0 & \text{on } \partial\Omega_p \setminus \cup_{i=1}^N \Gamma_i, \\ u_f = g & \text{on } \partial\Omega_f \setminus \cup_{i=1}^N \Gamma_i, \end{cases}$$

where g denotes a Dirichlet boundary condition imposed at the endpoints of the network. The problem in Ω_f is a prototype of flow or mass transport problem in a network of cylindrical channels, surrounded by the domain Ω_p where another flow and transport problem is defined. It is assumed that the interface between these regions is permeable, namely it is crossed by a normal flux proportional to $\kappa_i \left(u_p - u_f\right)$.

Applying the model reduction technique presented in Section 3, the equations defined on the network of inclusions Ω_f can be restricted to the one dimensional network Λ. Differentiation over the branches is defined using the tangent unit vector as $\partial_{s_i} w = \nabla w \cdot \boldsymbol{\lambda}_i$ on Λ_i, i.e. ∂_{s_i} represents the projection of ∇ along $\boldsymbol{\lambda}_i$. As a result,

the 3D-1D counterpart of problem (3.4) becomes

$$\begin{cases} a(u,v) + b_\Lambda(\overline{u},\overline{v}) = b_\Lambda(U,\overline{v}) & \forall v \in H_0^1(\Omega), \\ A(U,V) + b_\Lambda(U,V) = b_\Lambda(\overline{u},V) + \mathcal{F}(V) & \forall V \in H_0^1(\Lambda), \end{cases} \tag{7.1}$$

where $U, V \in H_0^1(\Lambda)$ denote trial and test functions relative to the reduced problem, with the following bilinear forms:

$$a(w,v) = (\nabla w, \nabla v)_\Omega, \quad A(w,v) = \sum_{i=1}^{N} (\partial_{s_i} w, \partial_{s_i} v)_{\Lambda_i}, \quad b_\Lambda(w,v) = \sum_{i=1}^{N} \kappa_i (w,v)_{\Lambda_i}.$$

The right-hand side $\mathcal{F}(V)$ takes into account the boundary conditions on the network endpoints, after applying a suitable lifting. A central role in equation (7.1) is played by the restriction operator $\overline{(\cdot)}$ that is defined as:

$$\overline{w}^{(i)}(\boldsymbol{s}) = \frac{1}{2\pi R_i} \int_0^{2\pi} w\left(\Lambda_i(\boldsymbol{s}) + R_i \boldsymbol{n}_{\Lambda_i}(\boldsymbol{s},\theta)\right) d\theta\,.$$

The vector $\boldsymbol{n}_{\Lambda_i}(\boldsymbol{s},\theta)$ indicates a normal vector perpendicular to $\boldsymbol{\lambda}_i(\boldsymbol{s})$ and depending on an angle θ, such that the set $\{\boldsymbol{n}_{\Lambda_i}(\boldsymbol{s},\theta) \mid \theta \in [0,2\pi)\}$ describes a unit circle around $\Lambda_i(\boldsymbol{s})$ and perpendicular to $\boldsymbol{\lambda}_i(\boldsymbol{s})$. Taking these definitions into account, it becomes obvious that $\overline{w}^{(i)}$ represents an average value of w with respect to a circle of radius R_i around $\Lambda_i(\boldsymbol{s})$ and perpendicular to $\boldsymbol{\lambda}_i(\boldsymbol{s})$.

We solve problem (7.1) in the two test cases shown in Fig. 5. In all cases, we enforce the value $u_f = g = 1$ at the inflow (a single point on one face of the cube) and $u_f = g = 0$ at one or several outflow points (that are visible on the opposite face of the cube in Fig. 5).

The results of the simulations are depicted in Fig. 6 in the left and right panels respectively. The test case of the single segment confirms the expected behaviour of the model. The field u diffuses radially from the line source. The effect of the variation of U on the line source is also visible. The second test case shows the ability of the method and of the corresponding finite element solver to handle more complex configurations. In this case, the network consists of a unit cube $\Omega = (0,1)^3$ that embeds an idealized branching network of 22 branches, visualized in red. For simplicity, the capillary radius and the parameter κ are kept constant for each branch and set to $R = 0.01$ and $\kappa = 0.1$. As a result, the solution u_f is expected to vary along Λ as shown in Fig. 6. The solution in Ω behaves correspondingly, as the solution of a Poisson equation with a constant concentrated source distributed on Λ.

8. Conclusion

Thanks to some emerging applications, such as the simulation of complex microvascular networks [3,4,12,27,28] or the computational study of plant roots [31], the numerical approximation of problems governed by partial differential equations featuring small

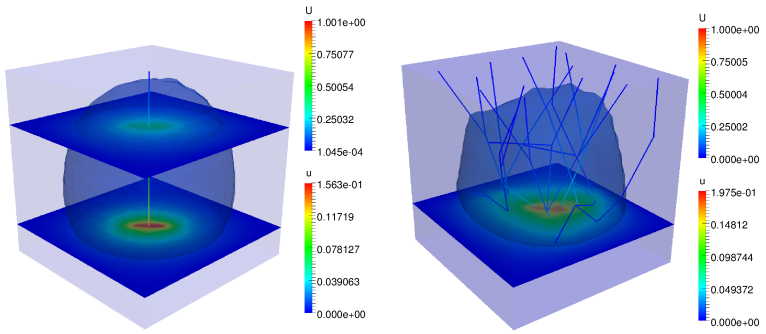

Fig. 6. Visualization of the numerical solutions U on Λ and u on Ω of problem (7.1) for the test cases of Fig. 5. The contour plots correspond to the solution values $u = 0.02$ (left) and $u = 0.01$ (right).

active inclusions, i.e. inclusions that actively interact with the surrounding environment, has recently attracted the attention of researchers in applied mathematics [5,7,19,6]. From the mathematical point of view, the problem consists of coupling partial differential equations on embedded manifolds with a dimensionality gap. The analysis and approximation of such problems is not completely established yet.

We believe that this work contains some significant contributions in this specific area. More precisely, we have proposed a new problem formulation, different from the one previously introduced by D'Angelo [5,7,6], that features the following advantages: (i) the new problem formulation naturally arises from the full three-dimensional description of the problem with inclusions, upon application of well defined model reduction hypotheses; (ii) it allows us to analyze the existence of solutions in the framework of Lax-Milgram Lemma; (iii) owing to (i), it is possible to provide upper bounds for the modeling error related to the model reduction strategy and to explicitly characterize the dependence of the model error from the parameters of the problem, such as the size of the inclusions; (iv) it allows us to study the approximation properties of the finite element method exploiting the classical Céa's approach. Combining this result with non-standard interpolation properties of functions with low regularity, we were able to prove error estimates for the proposed method in the case of uniform, δ-resolving and graded meshes. The extension of this approach to more advanced models, such as problems in mixed form [29] or time-dependent problems is under investigation and will be presented in forthcoming studies.

Acknowledgment

This work was partially supported by the Cluster of Excellence in Simulation Technology (EXC 310/2), by the DFG grant (WO/671 11-1) and by the (Italian) National Group for Scientific Computing, INDAM-GNCS.

References

1. F. Andreu, J. Mazón, and J. Rossi. The best constant for the sobolev trace embedding from $W^{1,1}(\Omega)$ into $L^1(\partial\Omega)$. *Nonlinear Analysis: Theory, Methods & Applications*, 59(7):1125–1145, 2004.
2. T. Apel, O. Benedix, D. Sirch, and B. Vexler. A priori mesh grading for an elliptic problem with dirac right-hand side. *SIAM Journal on Numerical Analysis*, 49(3):992–1005, 2011.
3. L. Cattaneo and P. Zunino. A computational model of drug delivery through microcirculation to compare different tumor treatments. *Int. J. Numer. Methods Biomed. Eng.*, 30(11):1347–1371, 2014.
4. L. Cattaneo and P. Zunino. Computational models for fluid exchange between microcirculation and tissue interstitium. *Netw. Heterog. Media*, 9(1):135–159, 2014.
5. C. D'Angelo. *Multi scale modelling of metabolism and transport phenomena in living tissues, PhD Thesis*. EPFL, Lausanne, 2007.
6. C. D'Angelo. Finite element approximation of elliptic problems with dirac measure terms in weighted spaces: applications to one-and three-dimensional coupled problems. *SIAM Journal on Numerical Analysis*, 50(1):194–215, 2012.
7. C. D'Angelo and A. Quarteroni. On the coupling of 1d and 3d diffusion-reaction equations: Application to tissue perfusion problems. *Mathematical Models and Methods in Applied Sciences*, 18(08):1481–1504, 2008.
8. B. Engquist, A. Tornberg, and R. Tsai. Discretization of dirac delta functions in level set methods. *Journal of Computational Physics*, 207(1):28–51, 2005.
9. L. Evans. Partial differential equations. *Graduate Studies in Mathematics*, 19, 1998.
10. L. Formaggia, A. Fumagalli, A. Scotti, and P. Ruffo. A reduced model for darcy's problem in networks of fractures. *ESAIM: Mathematical Modelling and Numerical Analysis*, 48(4):1089–1116, 2014.
11. S. Frei and T. Richter. A locally modified parametric finite element method for interface problems. *SIAM Journal on Numerical Analysis*, 52(5):2315–2334, 2014.
12. H. Frieboes, M. Wu, J. Lowengrub, P. Decuzzi, and V. Cristini. A computational model for predicting nanoparticle accumulation in tumor vasculature. *PLoS ONE*, 8(2), 2013.
13. D. Gilbarg and N. Trudinger. *Elliptic Partial Differential Equations of Second Order*, volume 224. Springer Science & Business Media, 2001.
14. V. Girault, K. Kumar, and M. F. Wheeler. Convergence of iterative coupling of geomechanics with flow in a fractured poroelastic medium. *Computational Geosciences*, 20(5):997–1011, 2016.
15. W. Gong, G. Wang, and N. Yan. Approximations of elliptic optimal control problems with controls acting on a lower dimensional manifold. *SIAM Journal on Control and Optimization*, 52(3):2008–2035, 2014.
16. C. Horgan. Eigenvalue estimates and the trace theorem. *Journal of Mathematical Analysis and Applications*, 69(1):231–242, 1979.
17. J. Jaffré and J. Roberts. Modeling flow in porous media with fractures; discrete fracture models with matrix-fracture exchange. *Numerical Analysis and Applications*, 5(2):162–167, 2012.
18. T. Köppl, E. Vidotto, and B. Wohlmuth. A local error estimate for the poisson equation with a line source term. In *Numerical Mathematics and Advanced Applications ENUMATH 2015*, pages 421–429. Springer, 2016.
19. T. Köppl and B. Wohlmuth. Optimal a priori error estimates for an elliptic problem with dirac right-hand side. *SIAM Journal on Numerical Analysis*, 52(4):1753–1769, 2014.

20. M. Kuchta, M. Nordaas, J. Verschaeve, M. Mortensen, and K. Mardal. Preconditioners for saddle point systems with trace constraints coupling 2d and 1d domains. *SIAM Journal on Scientific Computing*, 38(6):B962–B987, 2016.
21. J. Kuttler and V. Sigillito. An inequality for a stekloff eigenvalue by the method of defect. *Proceedings of the American Mathematical Society*, 20(2):357–360, 1969.
22. T. Köppl, R. Helmig, and B. Wohlmuth. A multi-scale model for mass transport in arteries and tissue. *Lecture Notes in Computational Science and Engineering*, 105:197–213, 2015.
23. T. Köppl, B. Wohlmuth, and R. Helmig. Reduced one-dimensional modelling and numerical simulation for mass transport in fluids. *International Journal for Numerical Methods in Fluids*, 72(2):135–156, 2013.
24. J. Li, J. Melenk, B. Wohlmuth, and J. Zou. Optimal a priori estimates for higher order finite elements for elliptic interface problems. *Applied numerical mathematics*, 60(1):19–37, 2010.
25. P. Macklin, S. McDougall, A. Anderson, M. Chaplain, V. Cristini, and J. Lowengrub. Multiscale modelling and nonlinear simulation of vascular tumour growth. *Journal of Mathematical Biology*, 58(4-5):765–798, 2009.
26. V. Martin, J. Jaffré, and J. Roberts. Modeling fractures and barriers as interfaces for flow in porous media. *SIAM Journal on Scientific Computing*, 26(5):1667–1691, 2005.
27. M. Nabil, P. Decuzzi, and P. Zunino. Modelling mass and heat transfer in nano-based cancer hyperthermia. *Royal Society Open Science*, 2(10), 2015.
28. M. Nabil and P. Zunino. A computational study of cancer hyperthermia based on vascular magnetic nanoconstructs. *Royal Society Open Science*, 3(9), 2016.
29. D. Notaro, L. Cattaneo, L. Formaggia, A. Scotti, and P. Zunino. *A Mixed Finite Element Method for Modeling the Fluid Exchange Between Microcirculation and Tissue Interstitium*, pages 3–25. Springer International Publishing, 2016.
30. S. Sauter and R. Warnke. Extension operators and approximation on domains containing small geometric details. *East West Journal of Numerical Mathematics*, 7:61–77, 1999.
31. N. Schröder, M. Javaux, J. Vanderborght, B. Steffen, and H. Vereecken. Effect of root water and solute uptake on apparent soil dispersivity: A simulation study. *Vadose Zone Journal*, 11(3), 2012.
32. N. Schwenck, B. Flemisch, R. Helmig, and B. Wohlmuth. Dimensionally reduced flow models in fractured porous media: crossings and boundaries. *Computational Geosciences*, 19(6):1219–1230, 2015.
33. L. Scott and S. Zhang. Finite element interpolation of nonsmooth functions satisfying boundary conditions. *Mathematics of Computation*, 54(190):483–493, 1990.
34. T. Secomb, R. Hsu, E. Park, and M. Dewhirst. Green's function methods for analysis of oxygen delivery to tissue by microvascular networks. *Annals of Biomedical Engineering*, 32(11):1519–1529, 2004.
35. O. Steinbach. *Numerical approximation methods for elliptic boundary value problems: finite and boundary elements*. Springer Science & Business Media, 2007.
36. K.H. Støverud, M. Darcis, R. Helmig, and S.M. Hassanizadeh. Modeling concentration distribution and deformation during convection-enhanced drug delivery into brain tissue. *Transport in Porous Media*, 92(1):119–143, 2012. cited By 9.
37. V. Thomée. *Galerkin finite element methods for parabolic problems*, volume Second Edition. Springer, 2006.

MOX Technical Reports, last issues

Dipartimento di Matematica
Politecnico di Milano, Via Bonardi 9 - 20133 Milano (Italy)

35/2017 Piercesare Secchi
On the role of statistics in the era of big data: a call for a debate

34/2017 Agosti, A.
Analysis of a Discontinuous Galerkin Finite Element discretization of a degenerate Cahn-Hilliard equation with a single-well potential

33/2017 Fumagalli, I.
A free-boundary problem with moving contact points

32/2017 Riccobelli, D.; Ciarletta, P.
Shape transitions in a soft incompressible sphere with residual stresses

31/2017 Schiltz, F.; Masci, C.; Agasisti, T.; Horn, D.
Using Machine Learning to Model Interaction Effects in Education: a Graphical Approach.

29/2017 Antonietti, P.F.; Mascotto, L.; Verani, M.
A multigrid algorithm for the p--version of the Virtual Element Method

30/2017 Bacchelli, V.; Micheletti, S.; Perotto, S.; Pierotti, D.
Parameter identification for the linear wave equation with Robin boundary condition

27/2017 Bonaventura, L.; Ferretti, R.; Rocchi L.;
A fully semi-Lagrangian discretization for the 2D Navier--Stokes equations in the vorticity--streamfunction formulation

28/2017 Pini, A.; Spreafico, L.; Vantini, S.; Vietti, A.
Multi-aspect local inference for functional data: analysis of ultrasound tongue profiles

26/2017 Masci, C.; Johnes, G.; Agasisti, T.
Student and School Performance in the OECD: a Machine Learning Approach.